J Mater Sci (2016) 51:3868–3879
DOI 10.1007/s10853-015-9706-5

Magnetically separable nitrogen-doped mesoporous carbon with high adsorption capacity

Tao Liang[2] · Fangxiao Wang[2] · Lin Liang[3] · Mengshuai Liu[2] · Jianmin Sun[1,2]

Received: 20 October 2015 / Accepted: 24 December 2015 / Published online: 4 January 2016

Abstract Magnetic mesoporous N-doped C (Fe_3O_4@N-mC) was obtained from the carbonization of mesoporous polyaniline Fe_3O_4@mPANI, which was fabricated by aniline directly polymerization around PVP-modified Fe_3O_4 particles. Surface modification and magnetic property were successfully introduced into the mesoporous C material with core–shell structure. Similar sizes of acidic methyl orange (MO), basic methyl blue (MB), and bulky-sized rhodamine B (RhB) were selected as target molecules to investigate the influences of molecular sizes and acidic-basic properties of the dyes on the adsorption behavior of Fe_3O_4@N-mC composite. Due to its spacious mesoporous structure and functional basic character, Fe_3O_4@N-mC composite displayed the adsorption ability in the order of MO > MB > RhB. The N-doped mesoporous C improved the adsorption to acidic dye compared with basic dye with the similar sizes. The adsorption kinetic was fitted with the pseudo-second-order model, suggesting that the chemical adsorption process was the rate-determining step for the whole adsorption process. The experimental adsorption capacities were well explained by the Langmuir model. Moreover, the introduced magnetic Fe_3O_4 made the composite easily separated from the solution after adsorption and regenerated with excellent stability. The fast and high adsorption performance, the easy separation, and excellent regeneration made Fe_3O_4@N-mC composite promising adsorbent candidate in practical wastewater treatment.

Tao Liang and Fangxiao Wang have contributed to this study equally.

✉ Jianmin Sun
sunjm@hit.edu.cn

[1] State Key Laboratory of Urban Water Resource and Environment, Harbin Institute of Technology, Harbin 150080, China

[2] The Academy of Fundamental and Interdisciplinary Science, Harbin Institute of Technology, Harbin 150080, China

[3] School of Life Science and Technology, Harbin Institute of Technology, Harbin 150080, China

Introduction

Organic dyes have been extensively used in many industries such as textile, paper, printing, food, and cosmetics [1, 2], which contribute to large and main pollutants in the aquatic ecosystem with over 7×10^5 tons produced annually [3]. The discharge of dyes into the environment was currently one of the world's major environmental problems for both toxicological and esthetic aspects. Various techniques have been reported for dye removal such as photocatalytic degradation [4], adsorption [5–7], and oxidation catalysis [8]. Among them, adsorption was considered as the most promising option for its efficient capacity, available/various adsorbents, easy operation, low-energy requirement, insensitivity to toxic substances, and no external formation of harmful substances [9]. Thus, selection of suitable adsorbent was the important guarantee for adsorption process.

Adsorbent structure, especially pore structure, was one important factor that affected the adsorption performance to pollutants. Commercial activated carbon was the most widely used adsorbent; however, restricted by its abundant microporous nature, large molecular pollutants could not easily penetrate its micropores and effectively adsorbed, resulting in the low adsorption capacity on the activated carbon [10, 11]. Mesoporous carbons materials with open pore structure and large pore size have shown remarkable improvement in the adsorption of bulky dyes [12]. For the

benefits of easy separation and the reuse of the adsorbent, the magnetic mesoporous carbon materials have been developed in pollution abatement [13]. Besides the pore structure, the surface chemistry of the adsorbent also played an important role in adsorption process [14]. The different classes of dyes had distinct adsorption behaviors on the adsorbent with different surface chemistry characteristics [15]. Due to the increased surface hydrophilicity, the oxygen-containing acid group mesoporous C improved the adsorption capacity to anionic dyes [16]. Peng et al. studied the effect of N-doped CMK-3, which was fabricated by ammonia treatment, on the adsorption to acid dye of black 1 and found the N-containing CMK-3 enhanced the interaction between carbon material and acid molecules [17]. However, the fabrication of N-functional mesoprous C still constituted a major challenge compared with easy synthesis of O-containing groups that were prepared by oxidation post-treatment [18]. Furthermore, there was little study on systematic adsorption influences of anionic/cationic or acidic/basic dyes on N-modified mesoporous carbon in comparison with the extensive O-containing mesoporous carbon. Various strategies were developed for the generation of N-containing surface groups, such as ammine post-treatment [19], chemical vapor deposition method [20], and carbonization of some containing nitrogen molecule [21]. However, the facile and direct synthesis of N-modified mesoporous carbon is attractive for practical applications.

Polyaniline (PANI), as the most commonly investigated azo polymer in that its low cost of monomer, easy polymerization, and high environmental stability, was attracted as favorable precursor to prepare N-modified carbon. In this contribution, magnetic mesoporous polyaniline composite (Fe_3O_4@mPANI) was synthesized by the polymerization of aniline with modified Fe_3O_4 particles using P123 and sodium dodecylsulfonate (SDS) as structure-directing agents. Thereafter, magnetic and N-functionalization were facilely and simultaneously introduced into the mesoporous C by carbonization of Fe_3O_4@mPANI to obtain the Fe_3O_4@N-mC composite. Fe_3O_4@N-mC was systematically investigated to adsorb various dyes of acidic methyl orange (MO), basic methylene blue (MB), and basic rhodamine B (RhB) with different sizes. Besides the surface composition effect, influences of solution pH and dye concentration on the adsorption performance were studied in detail. Moreover, the kinetic and equilibrium adsorption studies were conducted to clearly elucidate the adsorption mechanism for dye molecules. Moreover, the introduced magnetic property in N-doped mesoporous C made the absorbent easily separated after the adsorption by the external magnetic field. The efficient adsorption performance of mesoporous C coupled with N-containing group and magnetic functionalizations render Fe_3O_4@N-mC adsorbent appealing in the practical applications for the wastewater remediation.

Experimental section

Synthesis of magnetic N-doped mesoporous C (Fe_3O_4@N-mC) composite

Ferric chloride hexahydrate, sodium acetate, ethylene glycol, polyvinyl pyrrolidone (PVP), ammonium persulfate (APS), sodium dodecyl sulfonate (SDS), methyl orange (MO), methylene blue (MB), rhodamineB (RhB), and aniline were purchased from Sinopharm Chemical Reagent Co. Ltd., China. PEO_{20}-PPO_{70}-PEO_{20} (P123) was supplied from Sigma-Aldrich. All of the regents except aniline were of analytical grades and used as received without any further purification, and aniline was purified by twice distillations.

First, magnetic mesoporous polyaniline composite (Fe_3O_4@mPANI) was synthesized by one-step aniline polymerization around Fe_3O_4 particles formed beforehand. Then, Fe_3O_4@mPANI composite was carbonized to obtain N-modified magnetic mesoporous carbon denoted as Fe_3O_4@N-mC, the detailed synthesis procedure is shown in Scheme 1.

Synthesis of Fe_3O_4-PVP particles

Fe_3O_4 modified by PVP were synthesized by solvothermal method according to the previous work [22]. Ferric chloride hexahydrate (1.5 g), sodium acetate (2.0 g), and PVP (1.0 g) were dissolved into ethylene glycol (30 mL) under vigorous stirring. The homogeneous yellow solution was obtained and transferred to Teflon-lined stainless-steel autoclave for crystallization at 200 °C for 8 h, then the autoclave was cooled to room temperature. The obtained black magnetic particles were washed with ethanol several times and dried in vacuum at 60 °C for 12 h to obtain PVP grafted Fe_3O_4 particles denoted as Fe_3O_4-PVP. PVP acted as the linker to benefit the subsequent coverage of polyaniline shell around Fe_3O_4 core.

Synthesis of Fe_3O_4@mPANI and Fe_3O_4@N-mC

Fe_3O_4@mPANI composite was prepared by in situ polymerization of aniline in the presence of SDS and P123 mesostructure-directing agents. In a typical synthesis, the dilute HCl was first prepared by mixing 0.17 g 12 M HCl in 140 g deionized water. Then, P123 (0.15 g) and SDS (0.288 g) were dissolved into 100 mL the above HCl, then Fe_3O_4-PVP particles (0.10 g) were slowly added. The mixture was then ultrasonically dispersed for 30 min to

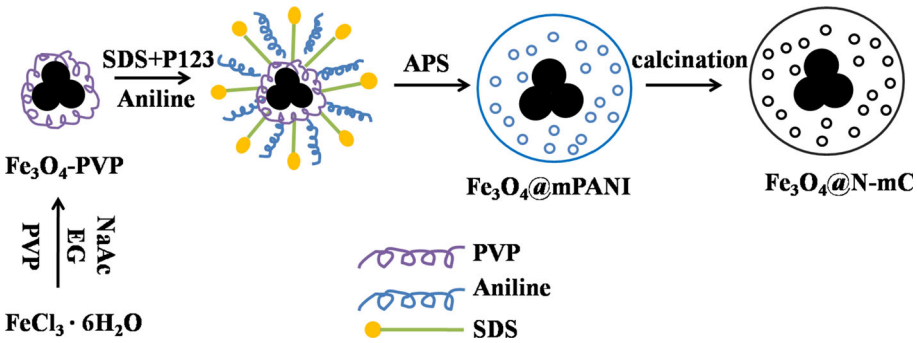

Scheme 1 Schematic illustration for the synthesis of Fe_3O_4@N-mC composite

obtain a uniform mixture. At the same time, aniline (0.187 g) was dispersed into the dilute HCl solution (40 mL) with magnetic stirring at room temperature for 30 min, then the solution was added into the above mixture under vigorous stirring to obtain a uniform mixture. The mixture was then placed in an ice-bath to maintain at 3–5 °C. Then an ice-cold APS aqueous solution (0.92 g in 100 mL) was dropped slowly and the mixture was stirred to become homogeneous. The polymerization was performed under mechanical stirring for 12 h at 3–5 °C. The resultant precipitates were washed with deionized water and ethanol several times. Thereafter, the solids were refluxed in ethanol solution of ammonium acetate to remove mesostructure-directing agents then dried in vacuum at 60 °C for 24 h to obtain the dark Fe_3O_4@mPANI composite.

Finally, the Fe_3O_4@mPANI composite was carbonized in a tube furnace under nitrogen with heating rate of 3 °C min^{-1} then maintained at 400 °C for 4 h and further programmed to 620 °C with 2 °C min^{-1} and kept at 620 °C for another 4 h. The black product was N-doped magnetic mesoporous carbon composite, designated as Fe_3O_4@N-mC.

Characterization

X-ray diffraction (XRD) pattern was obtained on Bruker D8 Advance X-ray powder diffractometer with Cu-Kα radiation (40 kV, 40 mA). Nitrogen adsorption/desorption isotherms were measured at −196 °C on ASAP 2020 volumetric analyzer. The surface area was calculated using BET method, the pore size distribution was derived from the desorption branch of the isotherms based on the BJH model, and total pore volume was determined from the amount of nitrogen adsorbed at P/P_0 ca. 0.99. Scanning electron microscopy (SEM) and EDX were recorded using a JSM-6700F scanning electron microscope. Transmission electron microscopy (TEM) was recorded on JEM-2010 electron microscope operating at 200 kV. Raman spectra were obtained on a LabRAM XploRA Raman microscope with 0.15 mW power and an argon-ion laser at excitation wavelength of 532 nm. The magnetization curve was measured on Quantum Design MPMS-7 SQUID magnetometer at 300 K under varying magnetic field. Adsorption amounts and equilibrium concentrations were quantified by Perkin Elmer Lambda 750 UV–Vis spectra. Fourier transform infrared spectroscopy (FTIR) was obtained on Perkin Elmer 100 spectrometer. X-ray photoelectron spectroscopy (XPS) measurements were recorded on Phi Quantera spectrometer with Al Kα radiation ($hv = 1486.6$ eV). pH_{pzc} values of adsorbent were determined using pH drift method by pH meter. Adsorbent was put in 100 mL 0.1 M NaCl solution, and the pH value of the mixture was adjusted to 2–12 using 0.1 M HCl or 0.1 M NaOH solution. Afterward, the flask was sealed and shaken in thermostat shaker for 48 h, the pH value of the mixture was measured and pH_{pzc} was taken as the point where the curve was zero. The zeta potential of the adsorbent was measured using dynamic light scattering analysis, the analysis was undertaken using a Malvern Zeta-sizer Nano zeta potential system.

Dye adsorption experiments

The acidic anionic dye MO, basic cationic dyes MB and RhB were selected as target molecules to investigate the dye adsorption behaviors on the magnetic N-doped mesoporous carbon composite. Their molecular sizes as well as structures were illustrated in Fig. 1.

Batch experiments for adsorption were performed in a set of flasks, each one containing 100 mL different initial concentrations of dyes and 10 mg adsorbent. The flasks were kept at 25 °C for 24 h to reach complete adsorption equilibriums. After that, the solution was filtered and the residual concentration was determined by UV–Vis spectra at the maximum wavelengths (λ_{max}) of light adsorption for each dye (665, 465, and 546 nm for MB, MO, and RhB, respectively). The adsorbed capacity at equilibrium was calculated through equation of $q_e = (C_0 - C_e)\frac{V}{m_s}$, where C_0 is the initial dye concentration (mg/L), C_e is the equilibrium concentration (mg/L), V is the volume of dye solution (L), and m_s is the adsorbent weight (g). The

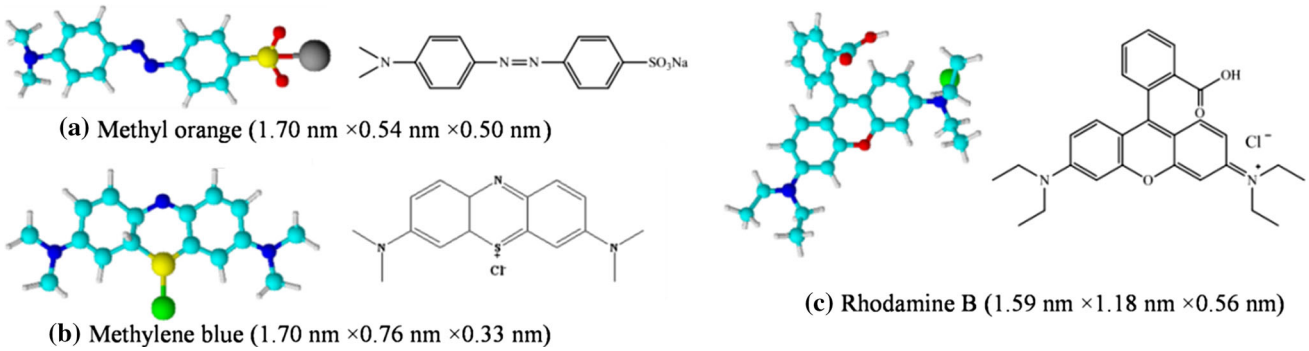

Fig. 1 Chemical formula and 3D representations of the selected dyes. Molecular sizes of the dyes were estimated using ChemSketch

sorption kinetics of the dyes were investigated using pseudo-first-order, pseudo-second-order, and intraparticle diffusion models. And the adsorption isotherms were analyzed by Langmuir and Freundlich model equations.

Regeneration of the adsorbent

To investigate the regeneration of the adsorbent, dye-loaded adsorbent was separated using an external magnet and then transferred into ethanol solution to release the adsorbed dye. Subsequently, the adsorbent was washed with deionized water and ethanol, then reused for another run directly.

Results and discussions

Structure, morphology, and magnetic properties of Fe_3O_4@N-mC composite

The crystalline nature and composition of the samples were characterized by XRD. Figure 2 showed the wide-angle XRD patterns of Fe_3O_4-PVP, Fe_3O_4@mPANI, and Fe_3O_4@N-mC samples. For Fe_3O_4-PVP, five diffraction peaks appeared at $2\theta = 30.0°$, 35.4°, 43.1°, 56.9°, and 62.5°, which were, respectively, corresponded to (220), (311), (400), (511), and (440) planes for the cubic lattice of Fe_3O_4 (JCPDS no. 19-0629). In the case of Fe_3O_4@mPANI, there were two new broad peaks observed at 20.6° and 25.6°. The peak centered at 20.6° was ascribed to periodicity parallel to the polymer chain, while the 25.6° peak was caused by the periodicity perpendicular to the polymer chain [23]. The wide-angle XRD pattern of Fe_3O_4@N-mC also showed a broad diffraction between 20 and 30° ascribed to the amorphous carbon, which proved that polyaniline was carbonized successfully. Furthermore, small angle XRD patterns (insert) of Fe_3O_4@N-mC sample exhibited one broad peak at ca. 2.4°, suggesting worm-like mesopores existence, in good

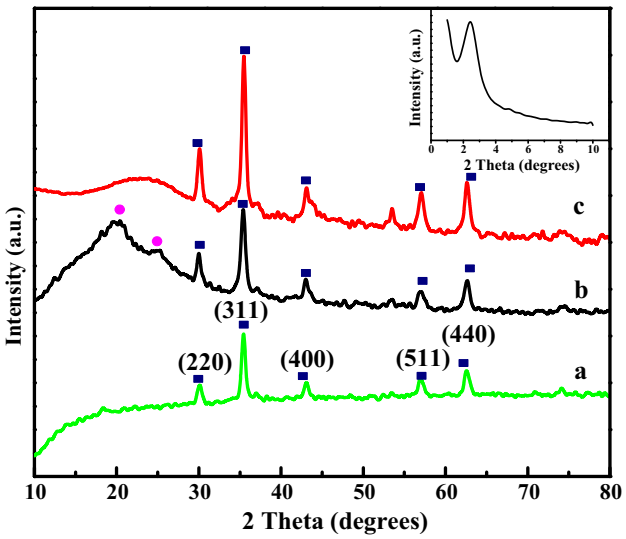

Fig. 2 XRD patterns of *a* Fe_3O_4-PVP, *b* Fe_3O_4@mPANI, and *c* Fe_3O_4@N-mC composite. *Inset* is the small angle XRD pattern for Fe_3O_4@N-mC sample

agreement with the mesostructured carbon material reported previously [5].

BET surface area and porous structure of Fe_3O_4@N-mC composite were provided by N_2 adsorption–desorption isotherms as shown in Fig. 3. Type IV isotherm with a distinct hysteretic loop between the relative P/P_0 pressure of 0.4-1.0 clearly verified the presence of mesopores in the composite. The BET surface area of Fe_3O_4@N-mC composite was 166.9 $m^2\ g^{-1}$, and the corresponding mesoporous sizes appeared at 3.2 nm and 6.0 nm.

The FTIR characteristic peaks of Fe_3O_4-PVP are displayed in Fig. 4a. The two peaks at 470 and 585 cm^{-1} were attributed to Fe–O stretching vibrations of Fe_3O_4 [21]. The peak at 1642 cm^{-1} was observed due to the carbonyl group of pyrrolidone on PVP chains, indicating that PVP was successfully grafted onto Fe_3O_4 surface. In the case of Fe_3O_4@mPANI composite, major bands were at 1605, 1494, 1296, 1235, and 1148, 830 cm^{-1}. The characteristic

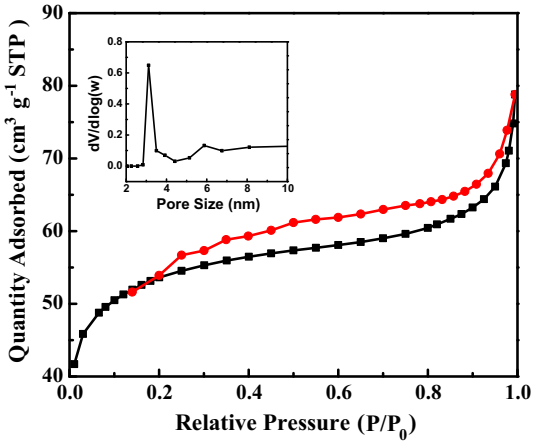

Fig. 3 Nitrogen adsorption–desorption isotherms of Fe_3O_4@N-mC composite. *Inset* is the pore size distribution

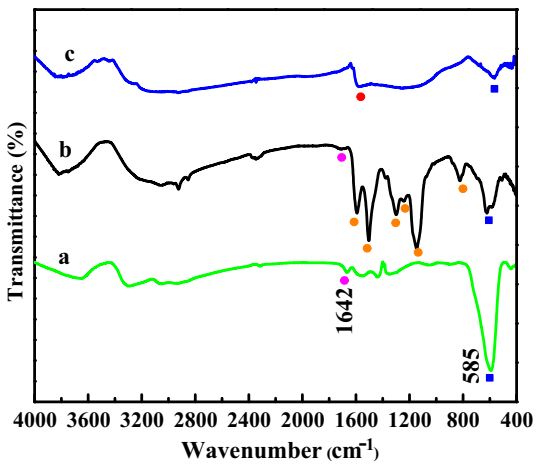

Fig. 4 FTIR spectra of (*a*) Fe_3O_4-PVP, (*b*) Fe_3O_4@mPANI, and (**c**) Fe_3O_4@N-mC composite

peaks at 1605 and 1494 cm^{-1} were assigned to the stretching vibrations of quinoid ring and benzenoid ring [22]. The peaks at 1296, 1235, and 1148 cm^{-1} were corresponded to C-N stretching vibrations [24]. The band at 830 cm^{-1} was ascribed to 1, 4-disubstituted benzene moiety [25]. Due to the carbonization process, the peaks characteristic of PANI became weaker or disappeared in Fe_3O_4@N-mC composite (Fig. 4c). The peak at 1590 cm^{-1} ascribed to $–NH_2$ deformation vibration demonstrated the successful N-functionalization on the composite surface [26]. Besides, the typical Fe–O stretching vibration of Fe_3O_4 at 585 cm^{-1} also proved the existence of Fe_3O_4 in the Fe_3O_4@N-mC composite.

XPS technique was powerfully used for the determination of surface composition for unique elemental markers of the material. The survey spectra of Fe_3O_4@N-mC composite are shown in Fig. 5a, which indicated the existences of C, O, N, and Fe elements. The binding energy of Fe2p was detected at 710.2 eV (insert), and N1 s spectra were deconvoluted into two peaks at about 400.5 and 399.2 eV, which were, respectively, assigned to the aromatic amine and the pyridine nitrogen in the Fe_3O_4@N-mC composite [27, 28]. XPS characterization further testified that N was successfully modified into the magnetic mesoporous C.

To gain more information of the carbon structure, Raman spectrum is measured in Fig. 6. The peak at 1348 cm^{-1} labeled as D-band was usually ascribed to the vibration of carbon atom with dangling mode for the in-plane terminations of disordered graphite. The peak at 1602 cm^{-1} labeled as G-band was due to the sp^2-bonded carbon–carbon stretching mode in a two-dimensional hexagonal lattice for graphene sheet [29]. Moreover, the G/D intensity ratio was regarded as a measurement for the graphitization degree [30]. For Fe_3O_4@N-mC composite, the I_G/I_D band ratio was ca. 1.56, higher than active carbon (AC) at 1.19, indicative of the improved graphitization degree in the Fe_3O_4@N-mC composite.

The morphology of Fe_3O_4@N-mC composite was further elucidated by SEM and TEM results. SEM images displayed the uniform and aggregated spherical morphologies (Fig. 7a, c). In TEM image, it was obviously observed that the spherical and agglomerated Fe_3O_4 particles were covered by light carbon shell layers of about 20–30-nm thickness. Besides, EDX analysis further evidenced the presence of N, O, Fe, and C elements in the Fe_3O_4@N-mC composite, consistent with the XPS results.

The magnetic behavior of the obtained material was investigated using vibrating sample magnetometer shown in Fig. 8. All the magnetic hysteresis loops were S-like curves, indicating that there were almost no remaining magnetizations when the external magnetic field was removed. At 25 °C, the saturation magnetization of Fe_3O_4-PVP particle was 76.8 emu g^{-1}. After polymerization of aniline, the saturation magnetization of Fe_3O_4@mPANI reduced remarkably to 13.4 emu g^{-1}, because Fe_3O_4 was encaged within the mesoporous polyaniline networks. Through the calcination of Fe_3O_4@mPANI, PANI was carbonized and the thinner carbon layer was formed, resulting in the increased saturation magnetization at 20.0 emu g^{-1} of Fe_3O_4@N-mC composite. The high saturation magnetizations were favorable for the easy separation of adsorbent from the solution after the adsorption by external magnetic field, which was very attractive to the practical applications.

Adsorption test and mechanism analysis

The capacities of various dyes adsorbed onto Fe_3O_4@N-mC and AC are shown as a function of time in Fig. 9. All the dyes were absorbed quickly by Fe_3O_4@N-mC

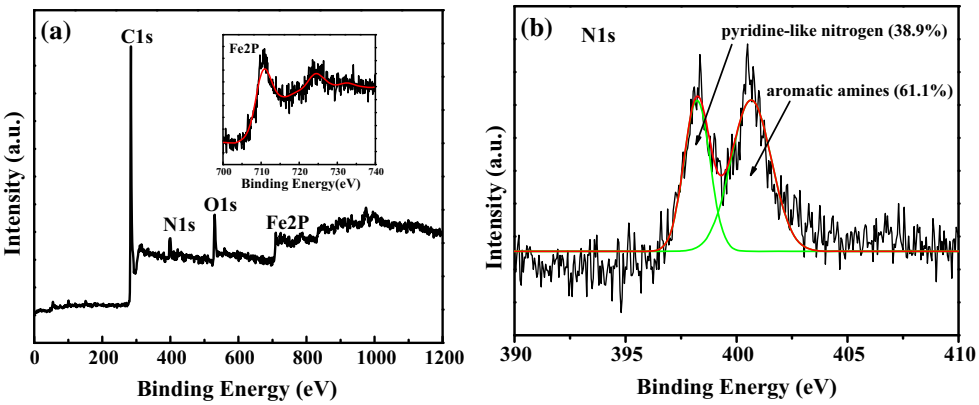

Fig. 5 **a** Survey XPS spectra, *inset* for enlarged Fe 2p spectrum and **b** N1s spectrum for Fe_3O_4@N-mC composite, the content percentage of the nitrogen functional groups was shown in *bracket*

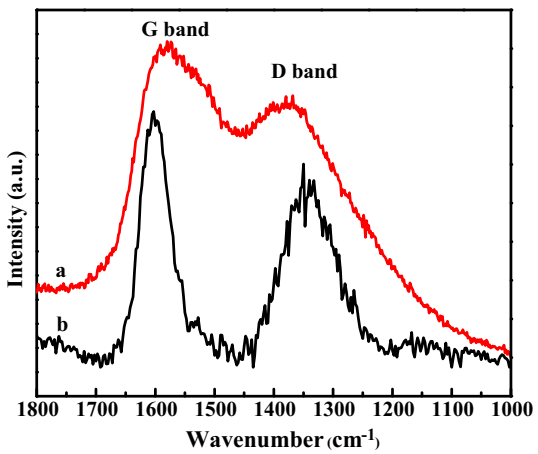

Fig. 6 Raman spectra of (*a*) Fe_3O_4@N-mC composite and (*b*) AC

composite within 10 min. Thereafter, adsorption capacity almost unchanged and achieved the equilibrium within 30 min. The sharp increase adsorption within the first 10 min was due to the abundant porosity of Fe_3O_4@N-mC. Although the commercial AC displayed much higher surface area at 430.8 $m^2\ g^{-1}$ than Fe_3O_4@N-mC at 166.9 $m^2\ g^{-1}$, the remarkable reduced adsorptions were observed on AC, suggesting the leading roles in adsorption behavior of the composite are porosity structure and surface composition. The dominant microporous nature of AC made the bulky-dye molecules difficultly penetrate into the pores and only adsorbed on the AC surface. In comparison with magnetic mesoporous C, the adsorption capacities of reported Fe_3O_4@mC [5] and Fe@MC [6] to RhB were higher than Fe_3O_4@N-mC, the high adsorption capacity was mainly ascribed to the high surface areas of the former two reference samples at 971 and 742 $m^2\ g^{-1}$, respectively. However, compared with other adsorbents although with high surface areas (Table 1), Fe_3O_4@N-mC exhibited higher adsorption capacity [2, 7, 31–33]. In the case of Fe_3O_4@N-mC, the adsorption capacity was in the order of MO > MB > RhB. Concerning the dye molecular size, it was understandable for the adsorption of RhB to need longer time and adsorption amount was significantly reduced compared with MO and MB. For similar molecular sizes of MO and MB, the acid–base properties of dyes affected the adsorption performances over the adsorbent. The adsorption capacity of acidic MO was higher than basic MB on Fe_3O_4@N-mC, which was explained that N-modified mC composite possessed basic property, which was favorable for the adsorption to acidic dye.

The solution pH significantly affected the adsorption extent [34], in order to investigate the pH influence, the surface charge of Fe_3O_4@N-mC composite via pH was conducted and pH_{pzc} was 8.95 (Fig. 10a). When $pH < pH_{pzc}$, the Fe_3O_4@N-mC surface became positively charged, while $pH > pH_{pzc}$, it was negatively charged. Moreover, the relationship of Fe_3O_4@N-mC zeta potential with pH showed that the isoelectric point was near to pH 8.85 (Fig. 10b). The zeta potential was positive at pH values lower than 8.85 and negative at pH values higher than 9. Figure 10c exhibited the adsorption behavior with different pH over Fe_3O_4@N-mC composite. In the case of cationic dyes MB and RhB, the adsorption capacities increased with pH increment. At low pH, cationic dyes were protonated in the presence of excess H^+ and the protonated dyes were more repulsed with positively charged absorbent, leading to the low adsorption capacity [35]. As $pH > pH_{pzc}$, the Fe_3O_4@N-mC surface became negative, the electrostatic interaction increased the cationic dyes of MB and RhB adsorptions [36]. Nevertheless, the opposite trend was observed for anionic dye MO adsorption. The maximum uptake value to MO solution appeared at low pH, the result was also well explained by electrostatic interactions between MO dye and adsorbent. At $pH < pH_{pzc}$, the adsorbent surface was positively charged, thereby increasing electrostatic attraction between MO molecular and the positively charged adsorbent and causing the high adsorption at low pH. With the gradual increase of the solution pH, the removal efficiency to MO decreased, which was attributed to the enhanced $OH^-$and

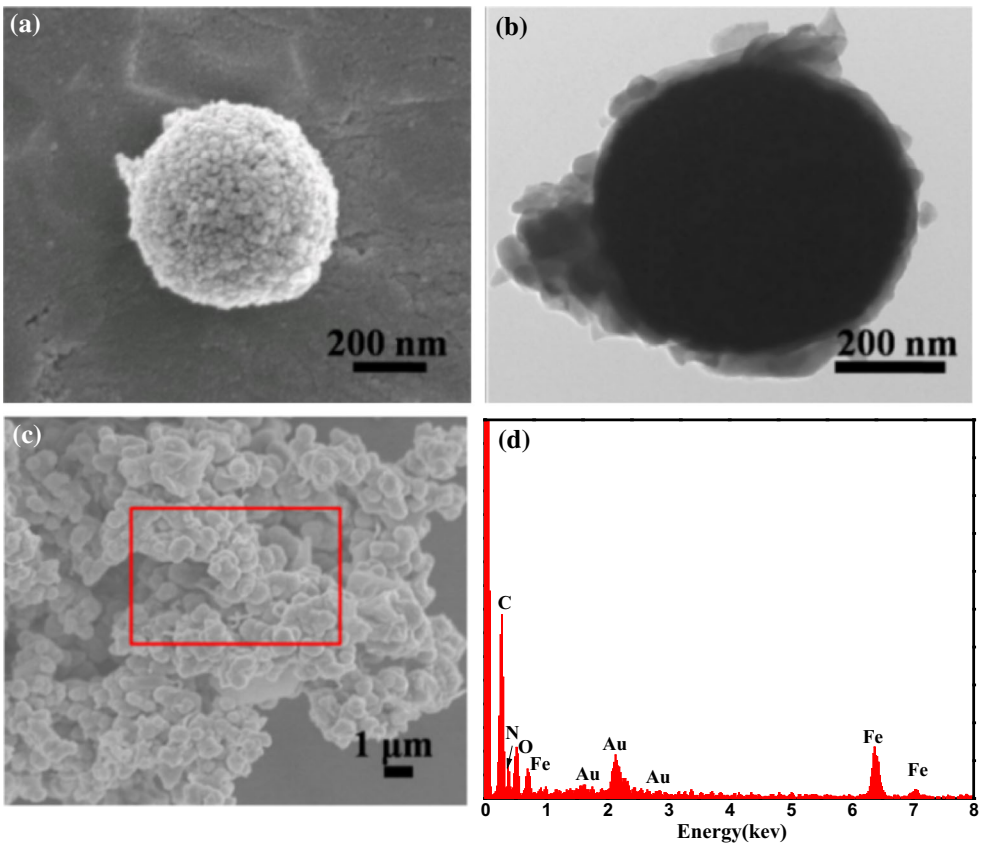

Fig. 7 **a**, **c** SEM images, **b** TEM image, and **d** EDX analysis for the rectangle area of Fe_3O_4@N-mC composite

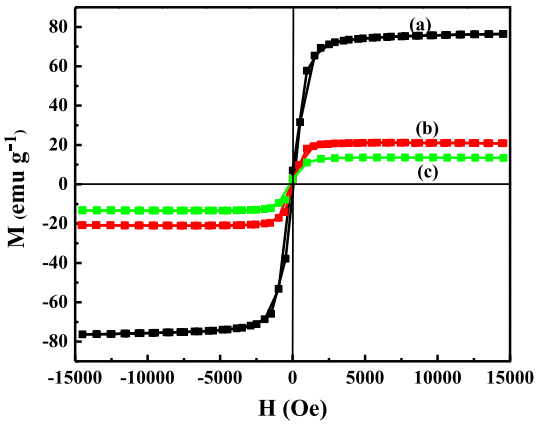

Fig. 8 Magnetic hysteresis loops of (*a*) Fe_3O_4-PVP, (*b*) Fe_3O_4@N-mC and (*c*) Fe_3O_4@mPANI composite

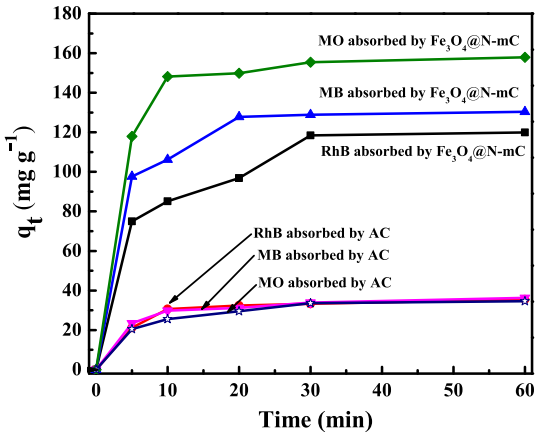

Fig. 9 Effects of contact time on the adsorption capacity ($T = 25$ °C, rpm = 120, pH 7.0, $C_0 = 20$ mg L^{-1})

more electrostatic repulsion between the negatively charged adsorbent and the anionic MO dye molecules [32, 37]. Hence, at $pH > pH_{pzc}$, the negatively charged Fe_3O_4@N-mC surface was favorable to the adsorption of cationic dyes, while at $pH < pH_{pzc}$, the positive-charged surface benefited the adsorption of anionic dyes. Based on the interaction between the adsorbent and dyes, it was comprehensible that at pH lower than 9, the adsorption capacity to MO was higher than MB and RhB, whereas the capacity to MB was higher than MO at $pH > 9$. The integrated influences of charge interaction and molecular size resulted in the similar adsorption behaviors to MO and RhB at pH 10.

To investigate the effect of dye concentration on the adsorption, batch experiments were carried out by adding 10 mg adsorbent to 100 mL different initial concentrations of dyes at 25 °C in Fig. 11. The adsorbed amounts of dyes improved with the initial concentration increasing. With

Table 1 Comparison of the adsorption capacities on various adsorbents

Adsorbent	Surface area	Adsorption capacity	Reference
Graphene/Fe_3O_4	–	29.70 mg g^{-1} for MB	[2]
Fe_3O_4@mC	971 m^2 g^{-1}	198.90 mg g^{-1} for RhB	[5]
Fe@mC	742 m^2 g^{-1}	~190 mg g^{-1} for RhB	[6]
MWCNT	–	102.30 mg g^{-1} for MB	[7]
Magnetic porous carbon	918 m^2 g^{-1}	73.00 mg g^{-1} for RhB	[31]
CMK-3	940 m^2 g^{-1}	24.58 mg g^{-1} for MO	[32]
NiO/MCM-41	435.9 m^2 g^{-1}	24.45 mg g^{-1} for MB	[33]

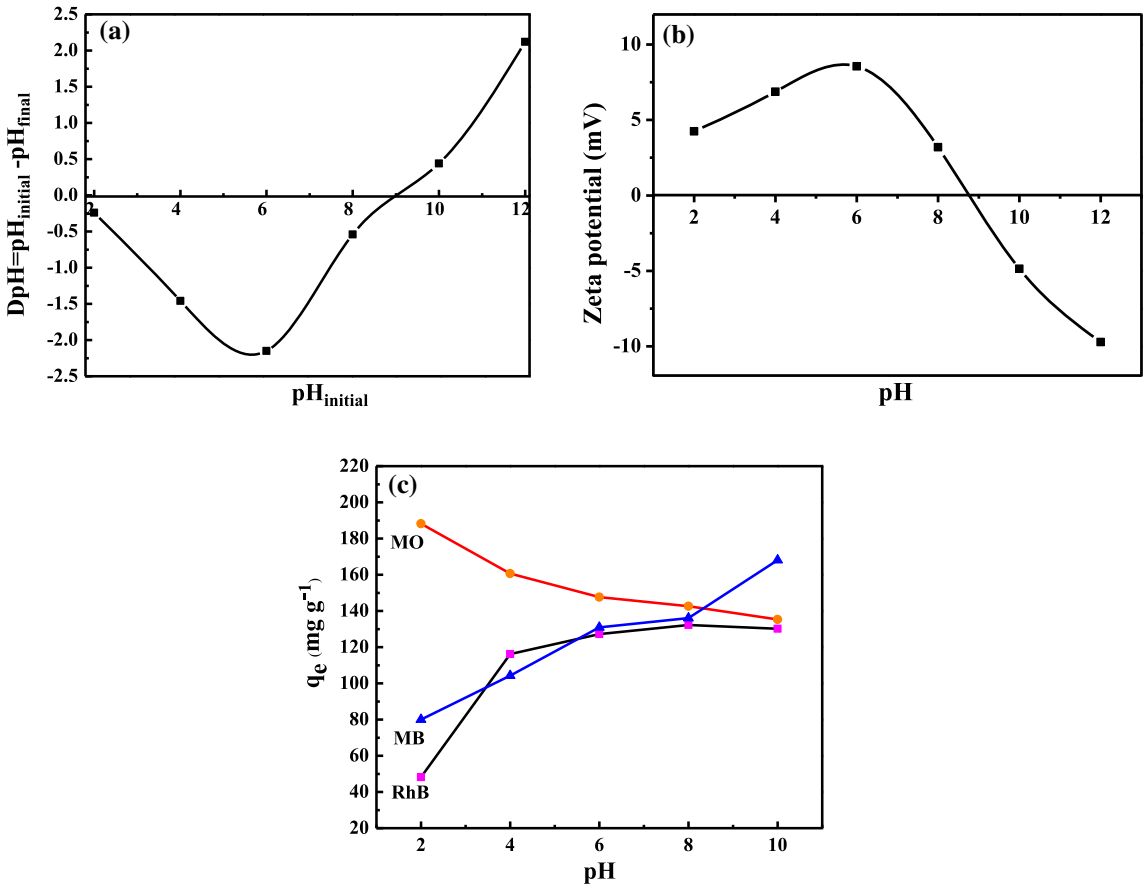

Fig. 10 **a** pH_{pzc} plot and **b** Zeta potential of Fe_3O_4@N-mC composite; **c** Effect of solution pH on the adsorption performance ($T = 25$ °C, rpm = 120, $C_0 = 20$ mg L^{-1})

the enhancement from 16 to 50 mg L^{-1}, the adsorbed equilibrium amounts were improved from 78 to 163 mg g^{-1} for RhB, 85 to 165 mg g^{-1} for MB, and 99 to 198 mg g^{-1} for MO adsorptions.

For the adsorbent, easy separation and recycling stability are the key factors for practical applications. The adsorption–desorption recycles are displayed in Fig. 12, which demonstrated that after five recycles Fe_3O_4@N-mC composite still kept good stability. The efficient adsorption property together with easy separation and excellent regeneration made Fe_3O_4@N-mC composite promising adsorbent candidate for the removal of organic dyes in wastewater.

Adsorption kinetics and adsorption isotherms

The adsorption equilibriums for various dyes over Fe_3O_4@N-mC composite were analyzed by Langmuir and Freundlich isotherm models and the corresponding parameters are listed in Table 2. All the adsorption results were more fitted Langmuir isotherm model with the best correlation regression coefficients than Freundlich model.

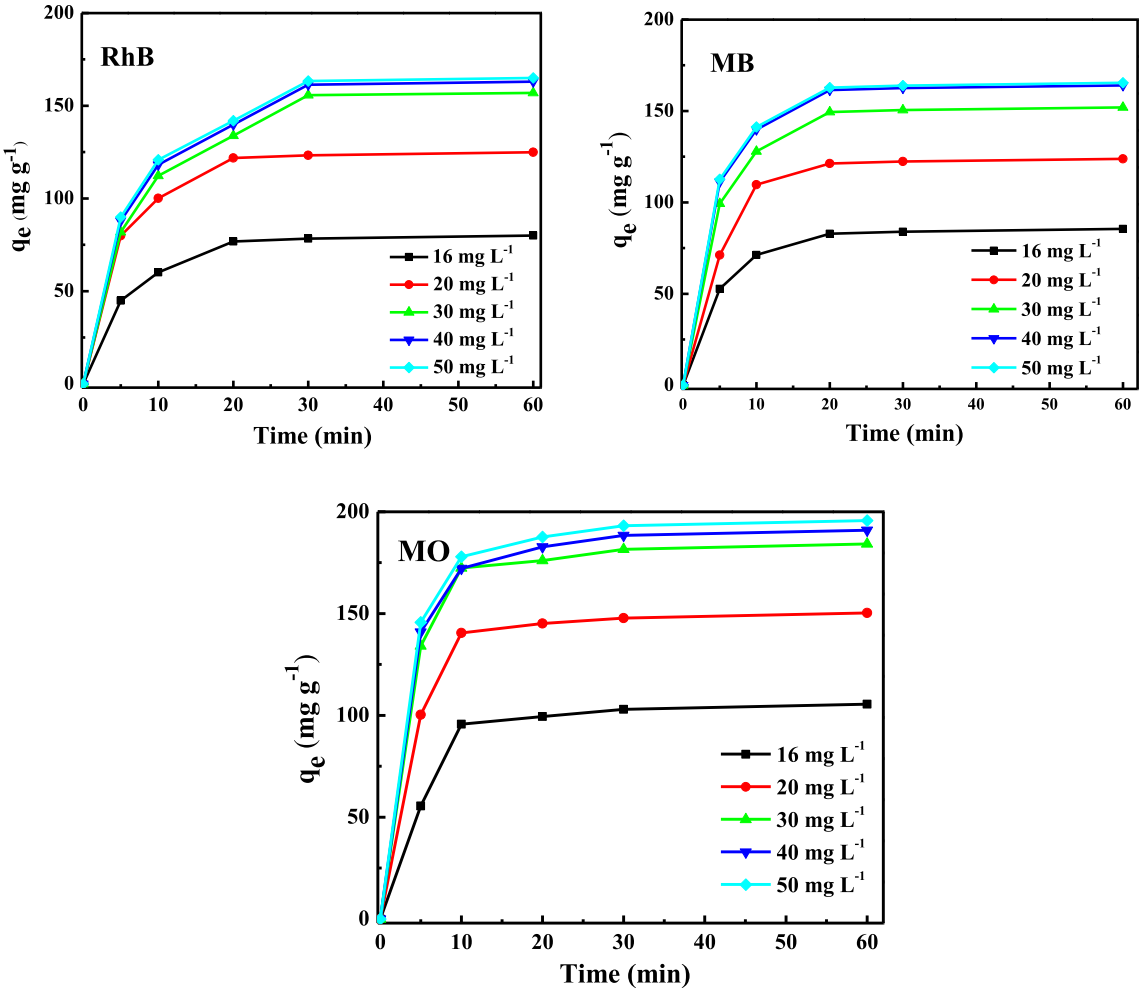

Fig. 11 The effect of initial dye concentration on the adsorption capacity ($T = 25$ °C, rpm = 120, pH 7)

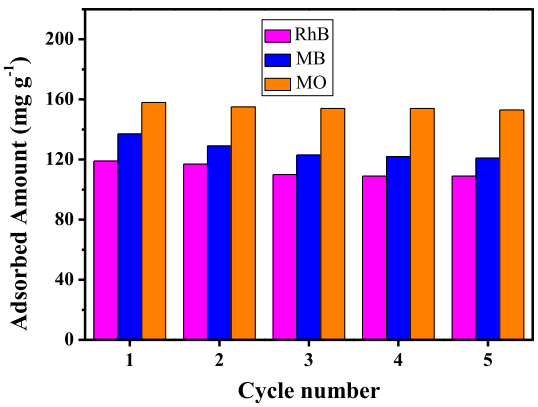

Fig. 12 The capacity of the adsorbed dyes over Fe_3O_4@N-mC composite in five cycles ($T = 25$ °C, rpm = 120, pH 7.0, $C_0 = 20$ mg L^{-1})

According to the Langmuir isotherm, the maximum adsorption capacities to RhB, MB, and MO were at 178.8, 185.1, and 200.0 mg g^{-1}, respectively, consistent with the experimental capacity order of MO > MB > RhB. Due to its basic property, N-modified mesoporous C resulted in stronger affinity to acidic dye of MO than to basic dyes of MB and RhB. Moreover, the higher K_L value and Langmuir constant further evidenced higher affinity to MO than to the other two dyes. Freundlich constant K_F was used as a relative measurement for the adsorption capacity and $1/n$ parameter was related to the sorption intensity [17]. The higher K_F value to MO also suggested that Fe_3O_4@N-mC possessed higher adsorption capacity to acidic dye than basic dyes. All $1/n$ values were less than 1, indicative of all the favorable adsorptions to various dyes on Fe_3O_4@N-mC composite [38].

The adsorption process generally includes three steps: (I) film diffusion; (II) intraparticle diffusion or pore diffusion, and (III) sorption onto interior sites [17]. In order to elucidate the adsorption rates over Fe_3O_4@N-mC composite, the kinetic data of adsorption were investigated by pseudo-first-order, pseudo-second-order, and intraparticle diffusion models (Table 3), respectively. It indicated that

Table 2 The isotherm parameters and correlation coefficients for the adsorption to various dyes over Fe_3O_4@N-mC composite

Dye	Langmuir			Freundlich		
	Q_m (mg g^{-1})	K_L (L mg^{-1})	R^2	1/*n*	K_F (mg g^{-1})	R^2
RhB	178.8	3.57	0.995	0.35	193.2	0.743
MB	185.1	3.60	0.999	0.24	207.4	0.779
MO	200.0	4.44	0.999	0.27	220.2	0.854

Table 3 The kinetic parameters for the adsorption to dyes over Fe_3O_4@N-mC

Dye	q_{exp} (mg g^{-1})	Pseudo-first-order			Pseudo-second-order			Intraparticle diffusion model		
		K (min^{-1})	q_e (mg g^{-1})	R^2	K_2 (10^{-3} g (mg min)$^{-1}$)	q_e (mg g^{-1})	R^2	K_i (g (mg min)$^{-1}$)	C	R^2
RhB	120.3	0.062	170.8	0.974	0.802	131.2	0.997	0.64	114.8	0.852
MB	131.5	0.038	159.1	0.825	2.61	137.7	0.997	0.75	124.7	0.983
MO	158.4	0.057	197.5	0.962	3.50	163.1	0.999	1.52	144.2	0.866

the calculated equilibrated adsorption amounts q_e and correlation coefficients R^2 values by pseudo-second-order model were more consistent with experimental q_e values than pseudo-first-order model. Thus, the pseudo-second-order kinetics model was more suitable to describe the adsorption kinetics data, revealing that adsorption rate was controlled by the chemical adsorption process. During the adsorption, chemical interaction between the adsorbent and dyes did work [39]. After the adsorption through surface reactions, dye molecules diffused into the adsorbent pores for further adsorption [40]. During this process, the intraparticle diffusion model [33] was used to identify the diffusion effects in adsorption process. In Fig. 13, there appeared two distinguishable intercepting lines, a fast increasing step at beginning, then a relatively slow increase and until equilibrium. The plots of q_t versus $t^{0.5}$ were linear relationships in the first rise period; moreover, the linear did not pass through the origin, suggesting that intraparticle diffusion was not the rate-controlling step during the whole adsorption process and some other factors might be involved [17]. The second portion in intraparticle diffusion model was the gradual equilibrated adsorption stage, which was resulted from the extremely low-dye concentration residual in the solution. For the intraparticle diffusion kinetic model in Table 3, K_i represents the intraparticle diffusion rate constant and C is the intercept. All R^2 by the intraparticle diffusion models were lower than those of the pseudo-second-order kinetics, further proving that the surface chemical interaction was suitable to the whole adsorption process besides the pore diffusion effects. The large and spacious mesopores of the composite benefited the dye diffusions to the adsorbent pores. Moreover, the surface interactions between adsorbent and dyes played the main roles in the whole adsorption process on Fe_3O_4@N-mC composite, basic N-functional mesoporous C improved the adsorption to acidic dyes.

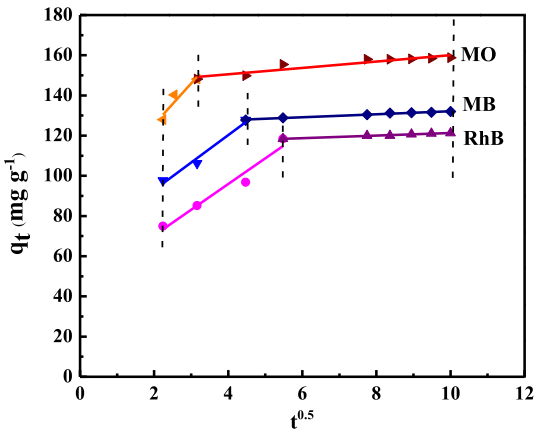

Fig. 13 Intraparticle diffusion model of adsorption dyes over Fe_3O_4@N-mC composite

Conclusion

Magnetic mesoporous polyaniline Fe_3O_4@mPANI was synthesized by aniline polymerization around Fe_3O_4 particles using P123 and SDS as mesoporous-directing agents, where magnetic Fe_3O_4 was encaged into the mesoporous polyaniline networks. Then basic N-doped magnetic mesoporous carbon (Fe_3O_4@N-mC) with core–shell structure was facilely obtained by the carbonization of Fe_3O_4@mPANI composite. Fe_3O_4@N-mC composite showed much higher adsorption rate than commercial AC and reference mesoporous C because of its spacious mesoporous structure and surface modification. Concerning the dye molecular size, it was understandable that the adsorption of bulky RhB needed longer time and adsorption amount was reduced compared with small-sized MO and MB. In the case of similar sizes of MO and MB, the

adsorption capacity to acidic MO was higher than basic MB over Fe_3O_4@N-mC composite, which was explained that basic Fe_3O_4@N-mC was favorable to the adsorption of acidic dye. The adsorption kinetic was fitted by the pseudo-second-order kinetics model, revealing that the overall rate of the adsorption process was controlled by the chemical adsorption interaction. Moreover, the experimental adsorption capacities were well fitted by the Langmuir adsorption model. Additionally, the introduced magnetic Fe_3O_4 rendered the Fe_3O_4@N-mC composite easily separated from solution by the external magnetic field. Furthermore, excellent reusability together with the fast and high adsorption performance made Fe_3O_4@N-mC composite promising candidate for efficient remediation of wastewater.

Acknowledgements We sincerely acknowledge the financial supports from National Natural Science Foundation of China (21373069), Science Foundation of Harbin City (NJ20140037), State Key Lab of Urban Water Resource and Environment of Harbin Institute of Technology (HIT2015DX08), and the Fundamental Research Funds for the Central Universities (HIT. IBRSEM. 201327).

References

1. Mezohegyi G, Zee FP, Font J, Fortuny A, Fabregat A (2012) Towards advanced aqueous dye removal processes: a short review on the versatile role of activated carbon. J Environ Manag 102:148–164
2. Ai LH, Zhang CY, Chen ZL (2011) Removal of methylene blue from aqueous solution by a solvothermal-synthesized graphene/magnetite composite. J Hazard Mater 192:1515–1524
3. Zhang YQ, Wang CC, Zhu T, Wang P, Gao SJ (2015) Ultra-high uptake and selective adsorption of organic dyes with a novel polyoxomolybdate-based organic-inorganic hybrid compound. RSC Adv 5:45688–45692
4. Wang FX, Liang L, Shi L, Liu MS, Sun JM (2014) CO_2-assisted synthesis of mesoporous carbon/C-doped ZnO composites for enhanced photocatalytic performance under visible light. Dalton Trans 43:16441–16449
5. Liang L, Zhu QC, Wang TB, Wang FX, Ma J, Jing LQ, Sun JM (2014) The synthesis of core-shell Fe_3O_4@mesoporous carbon in acidic medium and its efficient removal of dye. Microporous Mesoporous Mater 197:221–228
6. Wang TB, Liang L, Wang RW, Jiang YQ, Lin KF, Sun JM (2012) Magnetic mesoporous carbon for efficient removal of organic pollutants. Adsorption 18:439–444
7. Ghaedi M, Hajati S, Zare M, Zarec M, Jaberi SYS (2015) Experimental design for simultaneous analysis of malachite green and methylene blue; derivative spectrophotometry and principal component-artificial neural network. RSC Adv 5:38939–38947
8. Xu HY, Prasad M, Liu Y (2009) Schorl: a novel catalyst in mineral-catalyzed fenton-like system for dyeing wastewater discoloration. J Hazard Mater 165:1186–1192
9. Rivera-Utrilla J, Sánchez-Polo M, Gómez-Serrano V, Álvarez PM, Alvim-Ferraz MCM, Dias JM (2011) Activated carbon modifications to enhance its water treatment applications. J Hazard Mater 187:1–23
10. Moreno-Castilla C (2004) Adsorption of organic molecules from aqueous solutions on carbon materials. Carbon 42:83–94
11. He C, Hu XJ (2011) Anionic dye adsorption on chemically modified ordered mesoporous carbons. Ind Eng Chem Res 50:14070–14083
12. Derylo-Marczewsk A, Marczewski AW, Winter S, Sternik D (2010) Studies of adsorption equilibria and kinetics in the systems: aqueous solution of dyes-mesoporous carbons. Appl Sur Sci 256:5164–5170
13. Kyzas GZ, Deliyanni EA, Lazaridis NK (2014) Magnetic modification of microporous carbon for dye adsorption. J Colloid Interfaces Sci 430:166–173
14. Hadoun H, Sadaoui Z, Souami N, Sahel D, Toumert I (2013) Characterization of mesoporous carbon prepared from date stems by H_3PO_4 chemical activation. Appl Surf Sci 280:1–7
15. Órfão JJM, Silva AIM, Pereira JCV, Barata SA, Fonseca IM, Faria PCC, Pereira MFR (2006) Adsorption of a reactive dye on chemically modified activated carbons-Influence of pH. J Colloid Interfaces Sci 296:480–489
16. Dong X, Fu J, Xiong X, Chen C (2011) Preparation of hydrophilic mesoporous carbon and its application in dye adsorption. Mater Lett 65:2486–2488
17. Peng XM, Hu XJ, Fu DF, Lam FLY (2014) Adsorption removal of acid black 1 from aqueous solution using ordered mesoporous carbon. Appl Surf Sci 294:71–80
18. Bazula PA, Lu AH, Nitz JJ, Schueth F (2008) Surface and pore structure modification of ordered mesoporous carbons via a chemical oxidation approach. Microporous Mesoporous Mater 108:266–275
19. Kim W, Joo JB, Kim N, Oh S, Kim P, Yi J (2009) Preparation of nitrogen-doped mesoporous carbon nanopipes for the electrochemical double layer capacitor. Carbon 47:1407–1411
20. Xia YD, Mokaya R (2004) Synthesis of ordered mesoporous carbon and nitrogen-doped carbon materials with graphitic pore walls via a simple chemical vapor deposition method. Adv Mater 16:1553–1558
21. Sánchez-Sánchez A, Suárez-García F, Martínez-Alonso A, Tascón JMD (2014) Aromatic polyamides as new precursors of nitrogen and oxygen-doped ordered mesoporous carbons. Carbon 70:119–129
22. Zhu MY, Diao GW (2011) Synthesis of porous Fe_3O_4 nanospheres and its application for the catalytic degradation of xylenol orange. J Phys Chem C 115:18923–18934
23. Prathap MUA, Thakur B, Sawant SN, Srivastava R (2012) Synthesis of mesostructured polyaniline using mixed surfactants, anionic sodium dodecylsulfate and non-ionic polymers and their applications in H_2O_2 and glucose sensing. Colloid Surf B 89:108–116
24. Yan J, Wei T, Shao B, Fan ZJ, Qian WZ, Zhang ML, Wei F (2010) Preparation of a graphene nanosheet/polyaniline composite with high specific capacitance. Carbon 48:487–493
25. Liu H, Hu XB, Wang JY, Boughton RI (2002) Structure, conductivity, and themopower of crystalline polyaniline synthesized by the ultrasonic irradiation polymerization method. Macromolecules 35:9414–9419
26. Jia YJ, Jiang JC, Sun K (2015) Pyrolysis of polyaniline-poly(-styrene sulfonate) hydrogels to prepare activated carbons for the adsorption of vitamin B12. J Anal Appl Pyrol 111:247–253
27. Xu F, Minniti M, Barone P, Sindona A, Bonanno A, Oliva A (2008) Nitrogen doping of single walled carbon nanotubes by low energy N_2^+ ion implantation. Carbon 46:1489–1496
28. Sheng ZH, Shao L, Chen JJ, Bao WJ, Wang FB, Xia XH (2011) Catalyst-free synthesis of nitrogen doped graphene via thermal annealing graphite oxide with melamine and its excellent electrocatalysis. ACS Nano 5:4350–4358
29. Pimenta MA, Dresselhaus G, Dresselhaus MS, Cançado LG, Jorio A, Saito R (2007) Studying disorder in graphite-based systems by Raman spectroscopy. Phys Chem Chem Phys 9:1276–1291

30. Hu G, Cheng MJ, Ma D, Bao XH (2003) Synthesis of carbon nanotube bundles with mesoporous structure by a self-assembly solvothermal route. Chem Mater 15:1470–1473
31. Sun L, Tian CG, Wang L, Zou JL, Mu G, Fu HG (2011) Magnetically separable porous graphitic carbon with large surface area as excellent adsorbents for metal ions and dye. J Mater Chem 21:7232–7239
32. Mohammadi N, Khani H, Gupta VK (2011) Adsorption process of methyl orange dye onto mesoporous carbon material-kinetic and thermodynamic studies. J Colloid Interfaces Sci 362:457–462
33. Xiao XC, Zhang F, Feng ZP, Deng SJ, Wang YD (2015) Adsorptive removal and kinetics of methylene blue from aqueous solution using NiO/MCM-41 composite. Physica E 65:4–12
34. Gomez JM, Galan J, Rodríguez A, Walker GM (2014) Dye adsorption onto mesoporous materials: pH influence, kinetics and equilibrium in buffered and saline media. J Environ Manag 146:355–361
35. Alkan M, Dogan M, Turhan Y, Demirbas Ö, Turan P (2008) Adsorption kinetics and mechanism of maxilon blue 5G dye on sepiolite from aqueous solutions. Chem Eng J 139:213–223
36. Li W, Yue Q, Gao B, Ma Z (2011) Preparation and utilization of sludge-based activated carbon for the adsorption of dyes from aqueous solutions. Chem Eng J 171:320–327
37. Mahmoud DK, Mohamad AMS (2012) Batch adsorption of basic dye using acid treated kena fibre char: equilibrium, kinetic and thermodynamic studies. Chem Eng J 181:449–457
38. Ahmed SA, Soliman EM (2013) Silica coated magnetic particles using microwave synthesis for removal of dyes from natural water samples: synthesis, characterization, equilibrium, isotherm and kinetics studies. Appl Sur Sci 284:23–32
39. Hamzeh Y, Ashori A, Azadeh E, Abdulkhani A (2012) Removal of acid orange 7 and remazol black 5 reactive dyes from aqueous solutions using a novel biosorbent. Mater Sci Eng C 32:1394–1400
40. Kousha M, Daneshvar E, Dopeikar H, Taghavi D, Bhatnagar A (2012) Box-Behnken design optimization of Acid Black 1 dye biosorption by different brown macroalgae. Chem Eng J 179:158–168